



First principles modeling of the temperature dependent ternary phase diagram for the Cu–Pd–S system



William Paul Huhn^{a,*}, Michael Widom^a, Michael C. Gao^{b,c}

^a Department of Physics, Carnegie Mellon University, Pittsburgh, PA 15213, USA

^b National Energy Technology Laboratory, Albany, OR 97321, USA

^c URS Corporation, Albany, OR 97321, USA

ARTICLE INFO

Article history:

Received 25 September 2013

Received in revised form 27 May 2014

Accepted 30 May 2014

Keywords:

Bulk sulfidization

Sulfidization thresholds

First principles calculations

Phase stability

Phase diagram

Pd16S7

Pd4S

CuPdS

ABSTRACT

As an aid to the development of hydrogen separation membranes, we predict the temperature dependent phase diagrams using first principles calculations combined with thermodynamic principles. Our method models the phase diagram without empirical fitting parameters. By applying thermodynamic principles and solid solution models, temperature-dependent features of the Cu–Pd–S system can be explained, specifically solubility ranges for substitutions in select crystalline phases. Electronic densities of states calculations explain the relative favorability of certain chemical substitutions. In addition, we calculate sulfidization thresholds for the Pd–S₂ system and activities for the Cu–Pd binary in temperature regimes where the phase diagram contains multiple solid phases.

© 2014 Elsevier B.V. All rights reserved.

1. Introduction

Sulfidization impedes the use of palladium-based membranes for hydrogen sequester and capture. Due to the presence of hydrogen sulfide (H₂S) in any practical feed gas, sulfur rapidly covers the surface of the membrane, rendering its catalytic properties inert. Pure palladium membranes have limited application for hydrogen sequester and capture due to irreversible formation of bulk sulfides [1] and embrittlement due to lattice distortion caused by hydrogen atoms [2] diffusing through the bulk. Alloying palladium with other metals, such as silver [3] or gold [1], fixes many of the problems associated with palladium membranes, but these materials still suffer from sulfidization and are expensive. In the 2000s it was discovered that alloying palladium with copper [4,5] dramatically reduces the rate of sulfidization and further decreases the price of these membranes, though still not eliminating sulfidization. In order to realize hydrogen capture and sequester on an industrial scale, new membranes with different chemical compositions that resist sulfidization need to be devised, and their reactivity to sulfur needs to be examined. Computational methods

offer an attractive way to rapidly prototype different chemical families.

In this paper we computationally model the temperature-dependent phase diagram for the Cu–Pd–S system using first principles methods. Prior experimental work [6] determined the ternary phase diagram for the Cu–Pd–S system. We seek a simple and semi-quantitative model to gain insight into the essential features of the system, in contrast to complicated models with many fitting parameters that can yield close agreement with experiment at the cost of obscuring the underlying physics.

First, we describe our method for calculating ternary phase diagrams and apply it to Cu–Pd–S. Our model begins with first principles total energies, moves to focus on substitutional entropy, then examines vibrations. Comparison with experimental results shows general agreement. Certain details of energetics are explored through examination of the electronic density of states. We then apply our model to predict sulfidization thresholds for Pd interacting with S dimers and activities in Cu–Pd binaries.

2. Methods and calculations

In order to calculate a phase diagram using first principles methods, all plausible crystal structures must be considered, in principle. In the case of Cu–Pd–S, a wealth of experimental

* Corresponding author. Tel.: +1 (919) 660 5310.

E-mail addresses: wph@andrew.cmu.edu (W.P. Huhn), widom@andrew.cmu.edu (M. Widom).

crystallographic data gives an excellent starting point, especially for the binary compounds. We generalize these binaries to ternary structures formed from substitutions of the ternary species into either lattice sites or interstitial sites. Once the $T = 0$ K total energies for all likely crystalline structures have been calculated, it is straightforward to generate a $T = 0$ K phase diagram by creating the convex hull of total energies.

Subramanian and Laughlin [7] determined the phase diagram for Cu–Pd experimentally, and Li et al. created a CALPHAD model [8]. Above $T = 871$ K, the entire composition range of solid Cu–Pd exists in fcc solid solution. Below this temperature other solid phases are present. β -CuPd has a CsCl structure and exhibits a Cu-rich composition range extending to a composition of 58% Cu. Trimarchi and Zunger [9] showed using an evolutionary algorithm that first principles calculations predict cP2 to be the expected ground state at equiatomic composition. At copper concentrations near 75%, phases based on 1D and 2D long period superstructures (LPS) compete. Studies using ab initio methods to examine this region of the phase diagram have already been performed [10,11]. As we are primarily concerned with the palladium-rich side of the phase diagram, we only calculate the ideal 1D LPS, Cu₃Pd.tP28, (using a notation of [chemical formula].Pearson symbol) and ignore the 2D LPS and phase solubility ranges in the 1D LPS.

Determination of the phase diagram for Cu–S [12] using first principles calculations is problematic, as it contains an abundance of phases, many of which are non-stoichiometric or have large unit cells. We include only Cu–S structures with well-defined crystallographic refinements, as we do not expect this discrepancy to affect our results on the palladium-rich side of the phase diagram. The Pd–S phase diagram [13] is relatively simple, containing Pd₁₆S₇, Pd₄S, PdS, and PdS₂ phases as line compounds at low temperature, with Pd₃S stabilized at $T = 829$ K. We summarize the phase diagrams here only for comparison; our method does not require pre-existing knowledge of the phase diagrams.

In order to add temperature dependence to the phase diagrams, we introduce free energy models for select phases of interest, all of which are based on substitutional solid solution models with sublattice filling (where for some structures, the “sublattice” is the entire lattice). When calculating the ternary phase diagram and the activities, we work in the Gibbs ensemble, where we specify temperature, pressure, and chemical concentration. We neglect pressure dependence in the solid phases’ free energies, as solid compressibilities are low. Phonon free energies are included, in the harmonic approximation, giving free energies of form

$$G_{\text{tot}} = G_{\text{config}} + G_{\text{phonon}}. \quad (1)$$

Electronic free energy differences between competing phases of interest (Pd₁₆S₇ versus Pd₄S and well-ordered fcc-CuPd versus β -CuPd at 50% Cu), were found to be less than 1.5 meV/atom at temperatures as high as 1000 K. These differences are within the margin of error expected for our fits for analytic free energy models, and to simplify our modeling we have chosen to neglect G_{elect} .

For lattice models, two types of defects are common, substitutions and interstitials. Due to atomic size differences, the only interstitials expected to be relevant are sulfur interstitials in Cu–Pd phases. We calculate interstitial defect costs using the well-ordered structures Cu.cF4, Pd.cF4, Cu₅₀Pd₅₀.cF4, and CuPd.cP2, with sulfur occupying a single interstitial site for various supercell sizes. The least unfavorable substitution, octahedral in Cu₅₀Pd₅₀.cF4, lies approximately 2 eV above the convex hull with significant distortion, and thus we expect contributions to sulfur solubility by occupation of interstitials to be negligible.

We here summarize the configurational free energy G_{config} of a simple substitutional solid solution model, valid in the dilute limit. In a substitutional solid solution, we have a set of site classes i , each with N_i sites, an associated enthalpic cost of performing a

chemical substitution of species α into site class i , $\Delta E_{i,\alpha}$, and a substitution concentration of $x_{i,\alpha}$. In the substitutional solid solution model, it is assumed that each substitution is uncorrelated with all other chemical substitutions, and all spatial configurations have identical energies. This implies a linear dependence of ΔH with respect to composition, giving an enthalpic contribution of

$$\Delta H = \Delta H_0 + \sum_{i,\alpha} x_{i,\alpha} N_i \Delta E_{i,\alpha}, \quad (2)$$

where ΔH_0 denotes the enthalpy of the base structure with no substitutions. Including an ideal entropy of mixing

$$\Delta S = -k_B \sum_{i,\alpha} N_i [x_{i,\alpha} \log(x_{i,\alpha}) + (1 - x_{i,\alpha}) \log(1 - x_{i,\alpha})], \quad (3)$$

leads to a Gibbs free energy $\Delta G = \Delta H - T * \Delta S$. Here, ΔH_0 and $\Delta E_{i,\alpha}$ can be determined from first-principles calculations. However, we control only the total impurity concentration for a species α , x_α , not the number of substitutions in a given site class $x_{i,\alpha}$. Since we work with a fixed number of sites, we fix the total concentration of substitutions, and thus minimize the free energy over all $x_{i,\alpha}$ subject to the constraint of species number conservation.

To better elucidate the model, we restrict to the special case where only one type of substitution (with an enthalpic cost of ΔE) is allowed in only one sublattice containing N_0 sites. A case with two sublattices will be considered later. Other special cases include the binary regular solution model ($N = N_0$, where N is the total number of atoms) and the well-known binary ideal solution model ($N = N_0$, $\Delta E = 0$). The configurational free energy takes the form

$$\Delta G(N', T) = \Delta H_0 + \Delta E * N' + kT N_0 (x' \log x' + (1 - x') \log(1 - x')) \quad (4)$$

where N' is the number of substitutions performed and $x' = N'/N_0$ is the concentration of substitutions in the sublattice. The appropriate quantity to consider for thermodynamics is the free energy per atom, $\Delta g = \Delta G/N$, expressed in terms of the $x = N'/N$, which can be shown to be

$$\Delta g(x, T) = \Delta h_0 + \Delta E * x - T \Delta S \quad (5)$$

where $\Delta h_0 = \Delta H_0/N$, and $\gamma = N_0/N$ is a measure of the number density of sublattice sites. Of particular importance is the entropic contribution to the free energy,

$$-T \Delta S = k_B T \gamma (x \log x + (\gamma - x) \log(\gamma - x) - \gamma \log \gamma) \quad (6)$$

which we use for all phases modeled throughout this paper.

In order for a given substitution type to appreciably affect the free energy, the two necessary features are large γ values, corresponding to a sublattice dense in the total lattice and thus a significant entropic contribution from the sublattice, and small positive (or any negative) enthalpic cost Δh_0 for the substitutions, such that at a given temperature the entropic portion of the free energy can overcome the enthalpic cost (or reinforce the enthalpic gain).

We use VASP (the Vienna Ab-Initio Simulation Package) [14,15] a plane wave ab initio package implementing PAW potentials [16] to determine total energies. Previous work by Hu et al. [17] compared the accuracy of different pseudopotentials in the Pd–S system, and recommended PBEsol [18] as most suitable for calculations involving sulfur. The total energy calculations were performed by fully relaxing atomic positions and lattice parameters until energies converged to within 0.1 meV/atom. Subsequent convergence in k-point density was performed. A common energy cutoff of 273 eV was used. In order to model solubility ranges, calculations were performed both in unit cells and larger supercells. All phonon calculations were done using density functional perturbation theory, and were performed in at least a $2 \times 2 \times 2$

supercell of the unit cell, with the exception of Pd₁₆S₇.c146, where due to its large size only a 2 × 2 × 2 supercell of the primitive cell was used. Though a supercell method with chemical ordering is being used to model phonon free energies for certain disordered phases, Wu et al. [19] found that the high-temperature vibrational entropy difference between L1₂ and SQS8 configurations is only 0.03k_B, within their margin of error and corresponding to an upper bound on the free energy difference of 2.6 meV/atom at 1000 K. Table 1 shows a list of structures and their total energies.

3. Results and discussion

3.1. Phase diagrams

Given total energies, we calculate the enthalpy of formation for our structures at $T = 0$ K,

$$\Delta h = \Delta h_0 - \sum_i x_i \Delta h_i, \quad (7)$$

where Δh_0 is the calculated $T = 0$ K total energy for the base structure, x_i is the composition of a given species i in the structure, and Δh_i is the $T = 0$ K total energy for pure species i in a chosen reference structure. By convention, this reference structure is chosen to be the equilibrium structure at $T = 0$ K, so that at $T = 0$ K all enthalpies of formation for the pure species vanish. In the Cu–Pd–S system, the standard reference structures would be Cu.cF4 for copper, Pd.cF4 for palladium, and S.mp48 for sulfur.

As we are interested in interaction of gaseous sulfur with copper–palladium membranes, we have chosen to use gaseous sulfur dimers rather than the standard S.mp48 when calculating phase diagrams. In the case of the ternary phase diagram, all structures of interest have relatively low sulfur composition, so the mismatch in reference phase compared to experimental phase diagrams is negligible.

The quantity of importance for constructing temperature dependent phase diagrams is

$$dE = \Delta h - [\Delta h], \quad (8)$$

where $[\Delta h]$ is the enthalpy of formation of the convex hull at a structure's stoichiometry. By definition, this quantity is non-negative, and it vanishes only when the structure lies on the convex hull. This quantity is a measure of how far above the convex hull a

particular structure lies at $T = 0$ K. Structures with large dE 's require large entropic contributions to free energy in order to overcome enthalpic costs.

Fig. 1 shows the $T = 0$ K binary enthalpies of formation. Observe that palladium and sulfur react strongly, as can be seen by the maximum enthalpy of formation of 0.95 eV/atom. This strong enthalpy of formation reflects the tendency of pure palladium membranes to sulfidize. Next, copper and sulfur react almost as strongly, with a maximum enthalpy of formation of 0.82 eV/atom. Finally, copper and palladium have a maximum enthalpy of formation of only 0.12 eV/atom, indicating that the interspecies binding between copper and palladium is relatively weak. This is expected from the Cu–Pd phase diagram, as all known phases are variants of fcc (the $T = 0$, $p = 0$ structure for both Cu and Pd) or bcc (which is reached from fcc by a martensitic transition [38]). We find that the known structure CuS.oC24 is mechanically unstable, with an imaginary phonon mode that stabilizes a slight monoclinic distortion, and this distorted monoclinic structure, CuS.mC24, is the true ground state structure according to DFT. The stable phases predicted correspond to known low temperature stable phases, with the exception of CuS₂.tP12, which is not observed stable at temperatures as low as 300 K (its stability is mostly likely due to the use of S₂ as a reference structure), and CuS.mC24, the experimentally observed stable structure being CuS.hP12.

Experimental results [6] show Pd₁₆S₇.c146 and Pd₄S.tP10 having solubility ranges for copper, which implies the existence of substitutional or interstitial defects. Pd₁₆S₇.c146 contains four Wyckoff site classes: 8c and 24g sites containing palladium and 8c and 6b sites containing sulfur (see Fig. 2). For Pd₄S.tP10 there are only two site classes, an 8g containing palladium and 2a containing sulfur.

Shown in Fig. 3 is our calculated $T = 0$ K phase diagram for the Cu–Pd–S system (supporting data is in Table 2). We find the 8c site class in Pd₁₆S₇ is favorable to copper substitution. At $T = 0$ K it is enthalpically favorable to occupy 6 of the 8 possible lattice sites, with a sudden upturn for further filling of the 8c site class. The only other substitutions that are found favorable are S and Cu in β -CuPd, XCu in Pd.cF4, and Pd in CuS₂. Substitutions of Cu in the β -CuPd phase have a solubility range from 50% Cu to 55.5% at $T = 0$ K. We find the β -CuPd phase is only favorable to Cu substitutions on the Pd sublattice, and not Pd substitutions on the Cu sublattice, which is experimentally supported by observations that the

Table 1

A partial list of calculated structures, focusing on “base” structures with no substitutions. All energetic quantities are given in units of meV/atom. Cu₂Pd₃S₄ is a hypothetical structure based on Cu₂Pd₃Se₄.mp18 [37]. Cu.c12 is a hypothetical structure used to model the β -CuPd phase. ΔH and dE are defined in Eqs. (7) and (8).

Phase	Pearson symbol	Prototype	Group #	Space group	ΔH	dE
Cu [20]	cF4	Cu	225	Fm $\bar{3}$ m	0	0
Pd [21]	cF4	Cu	225	Fm $\bar{3}$ m	0	0
S ₂ Dimer	N/A	N/A	N/A	N/A	0	0
Cu ₃ Pd [22]	tP28	Cu ₃ Pd	99	P4mm	−103.0	0
CuPd	cP2	CuPd	221	Pm $\bar{3}$ m	−116.9	0
Cu ₂ S [23,24]	mP144	Cu ₂ S	14	P2 ₁ /c	−496.4	0
CuS [25]	oC24	CuS	63	Cmcm	−715.4	0
CuS ₂ [26]	cP12	FeS ₂	205	Pa $\bar{3}$	−821.5	0
Pd ₄ S [27]	tP10	Pd ₄ Se	114	P $\bar{4}$ 2 ₁ C	−418.9	0
Pd ₁₆ S ₇ [28]	c146	Pd ₁₆ S ₇	217	I $\bar{4}$ 3m	−589.7	0
PdS [29]	tP16	PdS	84	P4 ₂ /m	−892.8	0
PdS ₂ [30]	oP12	PdSe ₂	61	Pbca	−952.4	0
CuS [25]	hP12	CuS	120	I $\bar{4}$ c2	−712.9	2.5
Cu ₂ S [31]	tP12	Cu ₂ S	96	P4 ₃ 2 ₁ 2	−479.3	3.3
Cu ₄ Pd [32]	cP4	AuCu ₃	221	Pm $\bar{3}$ m	−99.7	3.4
Pd ₃ S [33]	oC16	Pd ₃ S	40	Ama2	−492.8	8
Cu ₅₀ Pd ₅₀ [34]	cF4	Cu	225	Fm $\bar{3}$ m	−106.9	10
Cu ₄ Pd [35]	tP20	Cu ₄ Pd	84	P4 ₂ /m	−69.6	12.8
Cu ₂ Pd ₃ S ₄	mP18	Cu ₂ Pd ₃ Se ₄	14	P2 ₁ /c	−743.0	13.2
Cu ₂ S [36]	cF12	CaF ₂	225	Fm $\bar{3}$ m	−503.1	20.6
Cu	c12	W	229	Im $\bar{3}$ m	36.3	36.3

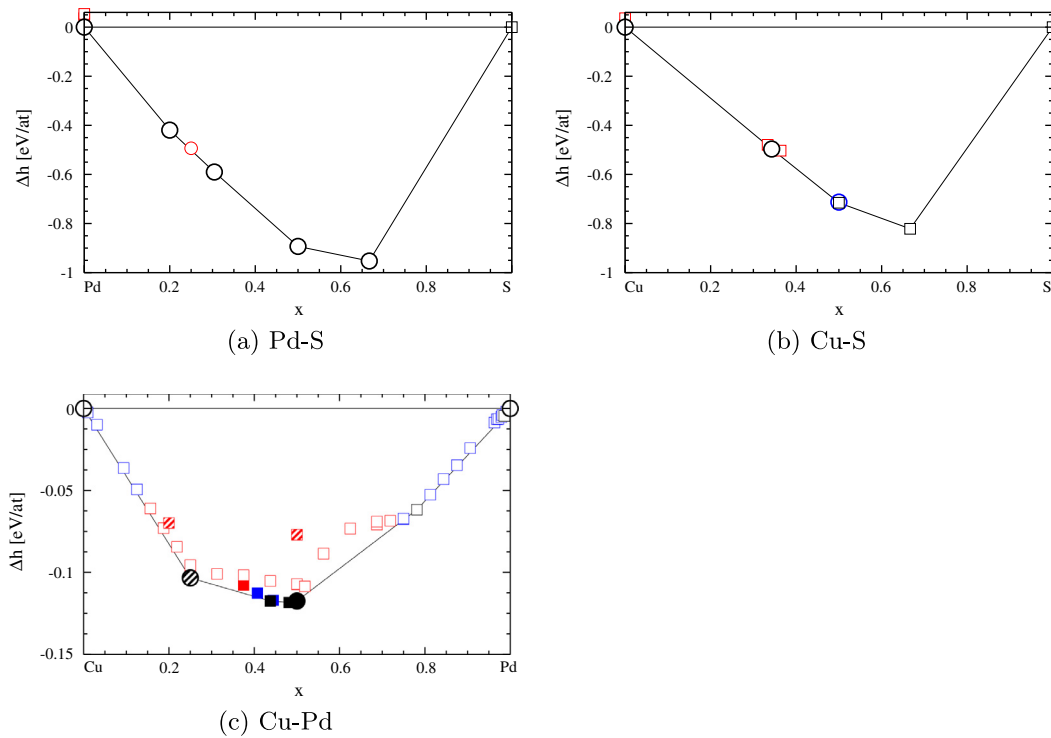


Fig. 1. Binary enthalpies of formation for Pd-S, Cu-S, and Cu-Pd. The x axis corresponds to concentration, and y axis corresponds to enthalpy of formation. Black symbols denote stable structures, blue correspond to structures within 3 meV of the convex hull, and red to structures above 3 meV. Circles with thick borders are known low temperature stable structures, circles with thin borders are known high temperature stable structures, and squares denotes all other cases (including hypothetical structures). For Cu-Pd, to better distinguish phases, filled symbols correspond to bcc structures, empty symbols to fcc, and dashed for the three other structures ($\text{Cu}_3\text{Pd.tP28}$, $\text{Cu}_4\text{Pd.tP20}$, and the SQS configuration for fcc at 50% Pd). (For interpretation of the references to color in this figure legend, the reader is referred to the web version of this article.)

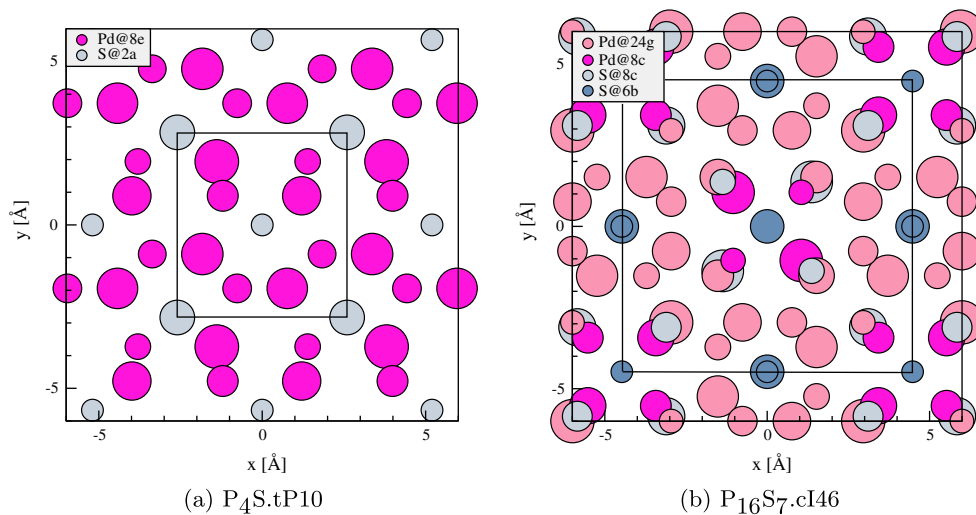


Fig. 2. Crystal structures for $\text{P}_4\text{S.tP10}$ and $\text{P}_{16}\text{S}_7.\text{cI46}$. The unit cells are outlined. Atomic sizes indicate vertical height.

palladium content of β -CuPd never exceeds 50%. As none of the Cu- and Pd- rich structures are in competition with $\text{CuS}_2.\text{tP12}$, and the entropic contribution is small, we ignore substitutions in $\text{CuS}_2.\text{tP12}$. We also find a small sulfur solubility range in the Cu sublattice of β -CuPd at $T = 0$ K, which is supported by experimental phase diagrams at $T = 673$ K and $T = 823$ K.

While these are the only stable $T = 0$ K substitutions, we expect that at higher temperatures, substitutions into other sites that had suitably low enthalpic cost will be stabilized by entropy: PdS.tP16 (2c), $\text{Pd}_{16}\text{S}_7.\text{cI46}$ (24g), and $\text{Pd}_4\text{S.tP10}$ (8e) sites being possible candidates (see Table 2). However, we chose to exclude modeling

the PdS.tP16 2c substitution range, as due to the small concentration of 2c sites in PdS.tP16 , combined with competition with other phases with strong entropic effects, we expect the concentration range to be negligible.

To determine solubility ranges more precisely, we model phases analytically (see Table 3), using first principles calculation data to suggest suitable enthalpic models. All models are based off the regular solution model, though with modifications to better reflect the behavior of the phase. We choose the models to smooth out fluctuations in the first principles calculated energies while still keeping the essential trends seen intact. The phases modeled are Pd_4S ,

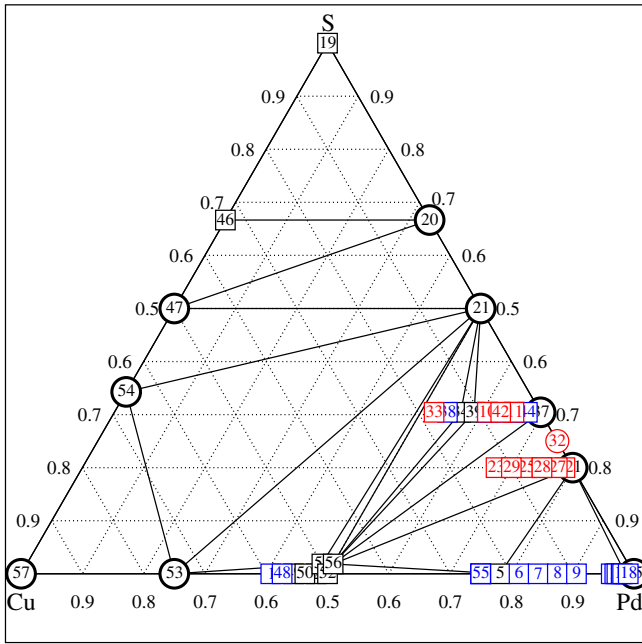


Fig. 3. The calculated $T=0$ K phase diagram for the Cu–Pd–S system. Plotting symbols as in Fig. 1.

Pd_{16}S_7 , $\beta\text{-CuPd}$, and the CuPd-FCC phase. In all cases we use the ideal entropy (Eq. (6)) for sublattice filling. Our model for Pd_{16}S_7 differs from a regular solution model in that we use a piecewise linear function (see Fig. 6) for the enthalpic part of the free energy. The enthalpic contribution to the free energy of Pd_{16}S_7 is increasingly favorable up to 6 substitutions ($x = 0.13$) on the 8c sublattice, but from 6 to 8 substitutions ($x = 0.174$) the favorability is reduced. Previous crystallographic work by Matkovic [28] observed a crystalline phase of Pd_{16}S_7 with 14% Cu concentration, the Cu occupying 8c sites. However this work was performed at 853 K and did not suggest any mechanism by which these substitutions are stabilized. For Pd_4S , we use the dilute limit form of the regular solution model ($1 - x \approx 1$), though it was necessary to add a small quadratic term to the free energy to fit our first principle results.

Both CuPd-FCC and $\beta\text{-CuPd}$ were fit using a first-order regular solution model, with CuPd-FCC having the entire lattice available for substitution, allowing usage of the standard form of a regular solution model. $\beta\text{-CuPd}$ has only the Pd sublattice available for substitution by Cu, which may be modeled using a regular solution model by replacing terms involving x with terms involving $x - 0.5$, where x denotes the Cu concentration. We also compute a SQS configuration for fcc at 50 Pd% [39] with purely random correlations until the 8th nearest neighbor and find it lies above the convex hull by 40 meV/atom.

Experimental phase diagrams show a sulfur solubility range near $\text{Cu}_{0.5}\text{Pd}_{0.5}$ trending in the palladium-rich direction. We find dilute S substitutions onto the Cu sublattice in $\beta\text{-CuPd}$, creating a phase trending in the palladium-rich direction, are stable at $T = 0$ K. Subsequent substitutions become rapidly unfavorable. From this, we expect limited entropic stabilization of additional substitutions of S in $\beta\text{-CuPd}$ at higher temperatures, leading to a roughly constant solubility range.

To include phonon free energy in solid solution phases, we calculate phonon free energies in the harmonic approximation at well-ordered configurations at select compositions and linearly interpolate between these compositions across the phase region. To model the free energy of gaseous sulfur, we use empirical data taken from the NIST-JANAF tables, as explained later in the paper.

Figs. 4 and 5 compare our calculated phase diagrams with experiment for $T = 673$ K and 823 K, respectively. Our $T = 673$ K phase diagram matches the experimental results qualitatively. Note, however, that the “ Cu_{2-x}S ” region of the experimental phase diagram contains multiple structures, many of which are non-stoichiometric, whereas ours contains only one structure. The phase labeled “ Cu_3Pd ” (or 1D LPS) has a slight solubility range experimentally whereas we model it as a well-ordered line compound. Our $T = 823$ K diagrams show more disagreement, as there is only one Cu–S structure that is stable and a Pd_3S structure is stabilized at this temperature. More recent phase diagrams have Pd_3S being stabilized at $T = 829$ K, however. This is likely due to entropic effects other than configurational and phononic (in the harmonic approximation) that were not included. As can be seen, Pd_3S is part of our collection of calculated structures but is not a stable low-temperature phase. At both temperatures we attempt to model sulfur solubility in the $\beta\text{-CuPd}$ phase but find sulfur solubility to

Table 2

A list of substitutions into binary structures to produce ternary structures. Only low enthalpic cost substitutions are shown. Impurity concentration denotes the concentration in the appropriate sublattice, not concentration in the structure as a whole.

Base structure	Site class	Chemical species change	Enthalpic cost (meV/atom)	Maximum impurity concentration in site class
$\beta\text{-CuPd}$	2a	Pd to Cu	0	12.5
$\beta\text{-CuPd}$	2a	Cu to S	0	3.8
$\beta\text{-CuPd}$	2a	Pd to S	0	3.8
Pd.cF4	4a	Cu to Pd	0	21.9
$\text{Pd}_{16}\text{S}_7\text{-cI46}$	8c	Pd to Cu	0	12.5
$\text{Pd}_{16}\text{S}_7\text{-cI46}$	24g	Pd to Cu	12.9	8.33
$\text{Pd}_4\text{S.tP10}$	8e	Pd to Cu	4.7	3.13
$\text{CuS}_2\text{-cP12}$	4a	Cu to Pd	0	6.25
PdS.tP16	2c	Pd to Cu	5.3	50.00

Table 3

Description of our phase models. γ denotes the number concentration of the sublattice in the total lattice and is used for scaling the entropic contribution to energy (see Eq. (6)). “Phonon concentrations” denotes the concentrations for which phonon free energies were calculated. x denotes the copper composition.

Phase	Substitution type (Cu composition range)	γ	Phonon concentrations	h_{config} (eV/atom)
Pd_4S	Cu@Pd8e (0–0.8)	8/10	0, 0.8	$-5.350 + 1.612x + 0.225x^2$
Pd_{16}S_7	Cu@Pd8c (0–0.175)	8/46	0, 0.175	$-5.237 + 1.445x(x < 6/46), -5.251 + 1.554x(x \geq 6/46)$
$\beta\text{-CuPd}$	Cu@Pd2a (0.5–1)	1/2	0.5, 1	$-4.8575 + 1.773(x - 0.5) + (x - 0.5)(1 - x)(-0.206(x - 0.5) - 1.526(1 - x))$
CuPd-FCC	Cu@Pd4a (0–1)	1	0, 0.50, 0.75, 1	$-5.477 + 1.469x + x(1 - x)(-0.529x - 0.267(1 - x))$

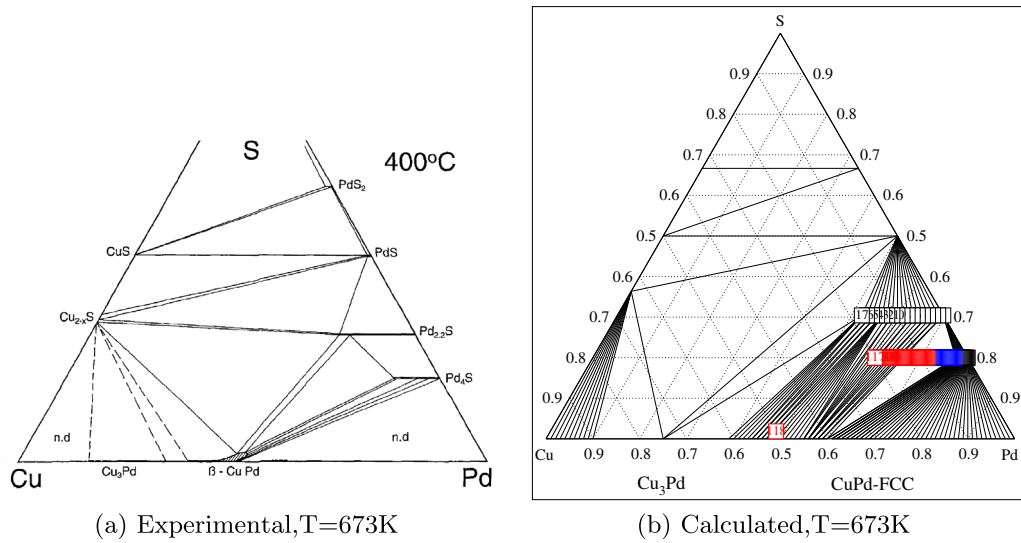


Fig. 4. The experimental phase diagram for the Cu–Pd–S system at $T = 673\text{ K}$, and our calculated phase diagram.

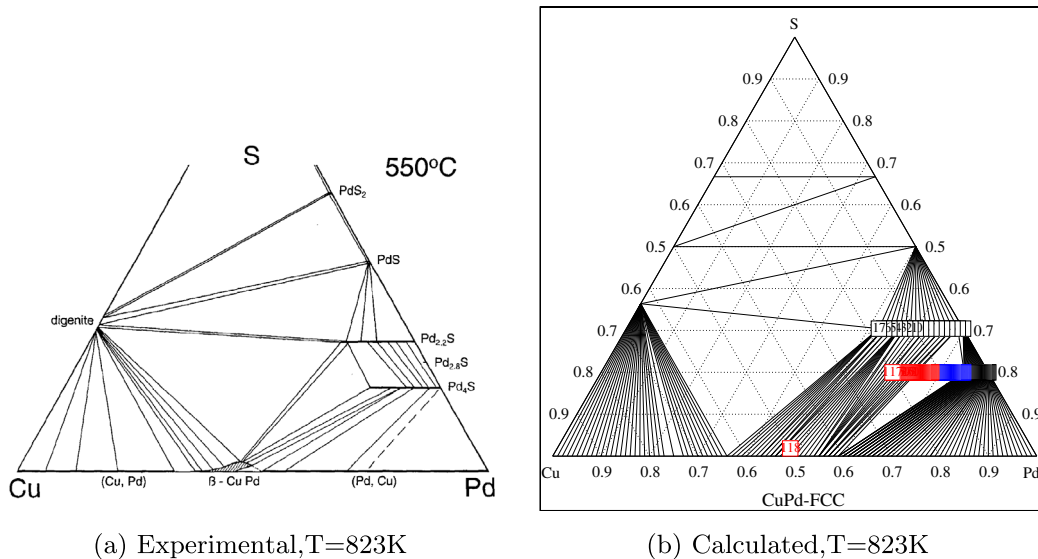


Fig. 5. The experimental phase diagram for the Cu–Pd–S system at $T = 823\text{ K}$, and our calculated phase diagram.

be unstable at temperatures of interest. This is surprising, as our $T=0\text{ K}$ phase diagram has a sulfur solubility range in $\beta\text{-CuPd}$ similar in shape to what is experimentally observed at higher temperatures, and the enthalpic behavior of our sulfur substitutions supports the observed temperature independence of the sulfur solubility range.

The $\text{Pd}_{16}\text{S}_7\text{.Cl}_{46}$ copper solubility range is not appreciably affected by the temperature, as it is dominated by enthalpy rather than entropy. The 24g site is unfavorable for copper substitution. The high multiplicity of the 24g site class gives a large entropic contribution to the free energy at high temperature relative to the 8c site class. However, we find that the enthalpic cost (see Fig. 6) associated with occupying 24g sites is too high relative to the entropic contributions at the given temperatures and only affects the solubility range by 1% to 2%. Thus the solubility range consists almost completely of 8c sites and is inappreciably affected by temperature. For this reason, our model (Table 3) only includes 8c sites and not 24g sites. For $\text{Pd}_{16}\text{S}_7\text{.Cl}_{46}$, at both measured temperatures the experimental copper solubility limit is 20%, and our calculated value is 17.5%, the mismatch likely due to Cu occupation

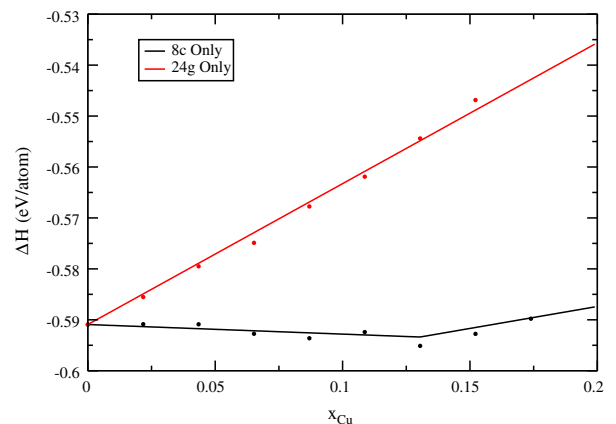


Fig. 6. Comparison for the enthalpy of formations for filling 8c sites versus filling 24g sites in $\text{Pd}_{16}\text{S}_7\text{.Cl}_{46}$.

of 24g sites. Our results explain why this solubility range appears to be independent of temperature; it is not stabilized due to entropic contributions but due to enthalpy arising from details of the electronic structure (see Section 3.2).

In contrast, Cu substitutions in Pd₄S.tP10 are not enthalpically favorable at $T = 0$ K but are entropically stabilized at higher temperature. As can be seen in the above phase diagrams, the copper solubility for Pd₄S.tP10 is temperature-dependent in both the calculated and experimental work. While our results agree qualitatively with experimental results, there is still a discrepancy in the copper solubility range. For Pd₄S.tP10, at $T = 673$ K the experimental value is 12.7% and ours is 2.5%, and for $T = 823$ K the values are 18.6% and 5% respectively. Solid solution models overestimate the configurational entropy, as including correlations between substitutions will alter the energies of distinct configurations with the same composition and reduce the multiplicity. We have thus overestimated the entropy of the Pd₁₆S₇ phase, whose solubility range extends to almost complete filling of the 8c site, relative to the Pd₄S phase, whose filling in the 8e sublattice is sparse. Thus we would expect more accurate free energy models will lead to decreased entropy in the Pd₁₆S₇ phase with comparatively small changes in Pd₄S, increasing the solubility range of Pd₄S. This will not affect the stability of Pd₁₆S₇ as it is primarily enthalpically stabilized.

The large solubility range in the palladium rich side of the CuPd-FCC phase at $T = 0$ K is also a factor in the incorrect solubility ranges for Pd₄S.tP10, as we have found that altering the fitting parameters for the CuPd-FCC phase appreciably affects the solubility range for Pd₄S.tP10. As we also encountered an issue with sulfur solubility in β -CuPd, with the sulfur solubility range destabilizing relative to CuPd-FCC at temperature below temperatures of interest, and we have a large solubility range on the Pd-rich side at $T = 0$ K for the CuPd-FCC phase, it appears that one major source of error is inaccurate modeling of the CuPd-FCC phase. We will return to this issue in the activities portion of this paper.

For our Cu–Pd binary at high temperatures, we find that Cu₃Pd.tP28 becomes unstable relative to the CuPd-FCC phase at $T = 827$ K, and β -CuPd becomes unstable relative to CuPd-FCC and Cu₃Pd.tP28 at $T = 536$ K and a composition of 59.5%, significantly below the experimentally observed temperature of $T = 871$ K but close to the experimental composition of 58%. This relative instability of β -CuPd at temperatures of interest is responsible for the observed instability of any sulfur solubility in β -CuPd in our $T = 673$ K and $T = 823$ K phase diagrams. We will show later that first-principles inspired corrections to the enthalpic portion of the free energy for CuPd-FCC will bring the phase transition closer in line with experimental results, though as CuPd-FCC phase has maximal entropy and β -CuPd phase (with only Cu substitutions in Pd sites) has minimal entropy in near the equiatomic composition region, it is likely that the assumption of ideal entropy in the FCC phase also plays a role.

But even with these discrepancies, it is clear that we have predicted major details of the Cu–Pd–S ternary phase diagram, specifically the mechanism for stabilization of the solubility ranges of Pd₄S.tP10 and Pd₁₆S₇ as well as details about the stability of the β -CuPd system, using only first principles calculations with no empirical fitting.

3.2. Electronic structure

The question remains why the Pd₁₆S₇.c146 8c site class favors copper in the first 6 substitutions, but substitution in the final two 8c sites are unfavorable. Consider the constituent binaries: copper binds less strongly with sulfur than palladium, and copper binding with palladium is relatively weak, so we would expect copper substitution into Pd–S binaries to be slightly unfavorable.

If it were to turn out to be favored, then we would expect Cu to fully occupy the 8c class. First-principles methods provide electronic structure information that can resolve this issue.

Fig. 7 shows the electronic densities of states for substitutions in Pd₁₆S₇.c146. Each colored solid line corresponds to the electronic density of states for a different number of substitutions in the 8c site class of Pd₁₆S₇.c146. It can be seen that the densities of states follow a rigid band model. Here copper is being substituted for palladium, and copper has one more electron in its valence shell than palladium. Under a rigid band model, performing a substitution adds one electron per unit cell without appreciably changing the valence electronic eigenstates, increasing the Fermi level relative to the fixed band structure.

In all cases, a pseudogap lies near the Fermi level. In the case of no substitutions, the pseudogap lies to the right of the Fermi level. As the number of copper substitutions increases, the increased electron count drive the pseudogap to the left, towards the Fermi level. At six substitutions the Fermi level lies almost directly at the minimum of the pseudogap. This is a well-known stabilization mechanism for alloys [40]. As the number of substitutions increases above six, the Fermi level is driven away from the pseudogap, destabilizing the structure and leading to the sudden increase in the enthalpy of formation (see Fig. 6). This pseudogap stabilization mechanism at $T = 0$ K, combined with large enthalpic cost of 24g substitutions, explains the temperature independence of the Pd₁₆S₇ solubility range.

3.3. Predominance diagrams

We now calculate the predominance diagram for the Pd–S₂ system. We work with a fixed quantity of palladium interacting with a reservoir of gaseous S₂, with temperature and pressure being free parameters. For an ideal gas, this implies that we control the chemical potential of the gas, and thus we work in the semi-grand canonical ensemble:

$$\Sigma(T, p, x) = G(T, p, x) - \mu_{S_2} N_{S_2} \quad (9)$$

where G is the previously defined Gibbs free energy, μ_{S_2} is the chemical potential for the sulfur dimers, and $N_{S_2} = N_S/2$ is the half the number of sulfur atoms in a given phase (as the chemical potential is for sulfur dimers). To determine sulfidization thresholds, we calculate the semi-grand canonical free energy for all phases of interest, Pd₄S.tP10, Pd₁₆S₇.c146, Pd₃S.oC16, and PdS.tP16. The phase with the lowest free energy will be stable. All Pd-containing phases of interest are line compounds, containing only total energy and phonon contributions.

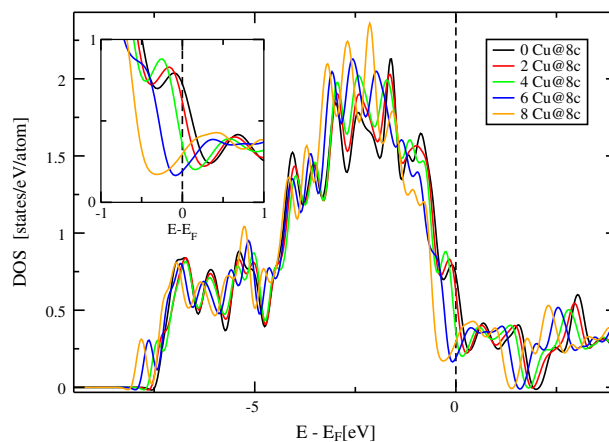


Fig. 7. Calculated electronic densities of states for Pd₁₆S₇.c146 with copper substitutions at the palladium 8c sites, with the Fermi level E_F (dashed line) set to zero. The inset enlarges the pseudogap region.

The chemical potential for S_2 complicates the calculation, as it is a gaseous phase. We incorporate empirical results into our method, in a manner consistent with the results obtained from first principles calculations. For the free energy of the gas, we have

$$\mu(T, p) = \mu^0(T) + kT \log \frac{p}{p_0}. \quad (10)$$

Here μ is the chemical potential per molecule, p_0 is a reference pressure (by convention taken to be 1 bar, as will be done here), and μ^0 is the chemical potential per molecule measured at the reference pressure,

$$\mu^0(T) = h - Ts|_{p=1}, \quad (11)$$

where H and S are obtained from the NIST-JANAF tables [41]. μ^0 obtained from the JANAF tables has a physically unrealistic infinite value at $T = 0$ K due to the presence of $1/T$ terms in both the H and TS contributions. As shown in Fig. 8, μ^0 is nearly linear for temperatures of interest, so we fit to a linear equation using the $770 \text{ K} < T < 1430 \text{ K}$ region to eliminate the $T = 0$ K pole. There is still an issue of constant offsets to energy; the JANAF tabulated values are relative to the enthalpy at $T = 298 \text{ K}$, and whereas all our calculated values are computed at $T = 0 \text{ K}$. In order to incorporate the empirical data into our method, we must shift its zero of energy. In particular, at $T = 0 \text{ K}$, we set the empirical data to match what first principles calculations would have predicted,

$$g_{S_2}|_{T=0 \text{ K}} = e_{\text{config}} + e_{\text{phonon}}|_{T=0 \text{ K}}. \quad (12)$$

As we have measured all energies relative to the tie-plane between pure elements, $e_{\text{config}} \equiv 0$, and so the zero-point energy e_{phonon} is the only contribution at $T = 0 \text{ K}$ taken from first principles calculations.

Shown in Table 4 are our predicted sulfidization thresholds relative to experimental predominance diagrams obtained by Taylor [42]. Predictions with and without phonon free energies are shown. It is necessary to include phonons to obtain reasonable agreement with experimental results, as when phonon free energies are excluded, the relative errors in pressure are as large as four orders of magnitude. When including phonon free energies, in all cases our pressure estimates are within a factor of 6 of experimental results. It should also be noted that Taylor's phase boundaries are themselves based on fits from experimental enthalpy data. One difficulty is that Taylor has a liquid region in the high-temperature, low pressure region of the predominance diagram, whereas we are only interested in solid phases, so experimental thresholds from the solid regions were extrapolated to liquid regions to give numbers suitable for comparison. This extrapolation is valid as Taylor's

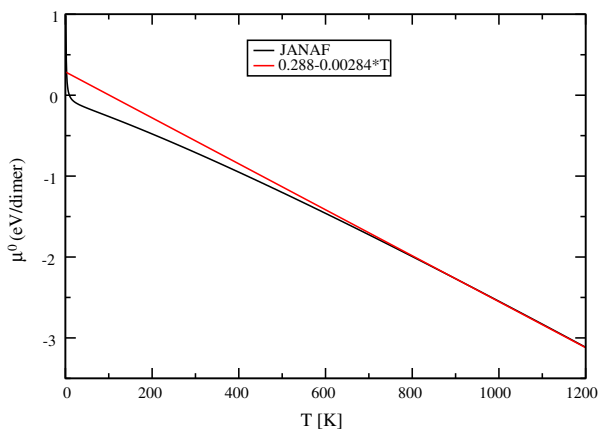


Fig. 8. The chemical potential of S_2 dimers. Black is NIST-JANAF, and red is our linear fit. (For interpretation of the references to color in this figure legend, the reader is referred to the web version of this article.)

thresholds in the solid regions were found to be extremely linear. Another difficulty is that Pd_3S is stable for a small pressure range in between temperatures of 830 K and 920 K, and it would likely be stable for higher temperatures if not for the liquid phase, but our calculations do not predict it stable in this region. This is most likely due to errors in the phonon free energy, which as already shown appreciably affects results.

3.4. Activity calculations

In this last section, the activities of species in binary Cu–Pd are calculated, as these can be used to predict sulfidization thresholds for Cu–Pd in the presence of S. We wish here to find the activities across the entire composition range with multiple phases.

The definition for the activity of a species A as a function of composition x_A , pressure P , and temperature T is [43]

$$\log a_A(x_A, P, T) = \frac{\mu_A(x_A, P, T) - \mu_A^0(P, T)}{k_B T},$$

where a_A is the activity for species A, $\mu_A(x_A)$ is the chemical potential for species A, and μ_A^0 is a reference chemical potential for species A. As we are specifying x_A , P , and T , the natural choice of thermodynamic potential is the Gibbs free energy,

$$G = G(N_A, N_B, p, T) = \mu_A N_A + \mu_B N_B,$$

where N_A and N_B are the total number of A and B atoms, respectively, and the thermodynamic derivative giving the chemical potential is

$$\mu_A(N_A, N_B, P, T) = \left. \frac{\partial G}{\partial N_A} \right|_{N_B, P, T}.$$

However, the quantity of importance for phase transitions is the Gibbs free energy per atom,

$$g = g(x_A, P, T) = \frac{G(N_A, N_B, P, T)}{N_A + N_B}.$$

We may express the chemical potential in terms of intensive quantities as

$$\mu_A(x_A, P, T) = g + (1 - x_A) \left. \frac{\partial g}{\partial x_A} \right|_{P, T},$$

where x_i is the composition of species i , and we have chosen to parameterize the free energy by the composition for A. Similarly,

$$\mu_B(x_A, P, T) = g + (1 - x_B) \left. \frac{\partial g}{\partial x_B} \right|_{P, T} = g - x_A \left. \frac{\partial g}{\partial x_A} \right|_{P, T}.$$

These activities depend only on the free energy and the derivative of the free energy at a given composition. They are piecewise analytic functions across the composition range, completely determined by the thermodynamically stable phase at that composition. The activities can therefore be viewed as alternative representation of the underlying phase diagram for the system. They are discontinuous only when the derivative of the free energy changes (the free energy itself must always be continuous, due to the requirement of convexity).

As mentioned before, we believe the magnitude of the calculated free energy of our fcc phase is artificially large, destabilizing the β phase, and thus any calculated activities would be flawed near the 50% Cu region of the phase diagram. To support this assertion, here we refit the fcc phase using only low-solubility first principles data on either side of the composition range. This reduces the magnitude of the free energy of the fcc phase while still using first principles derived calculations. This should not be viewed as abandoning our pure first principles phase diagram as shown before, but rather a correction inspired by known experimental

Table 4

Sulfidization threshold pressures for the Pd–S₂ system. Calculated values with and without phonon contributions are separately shown. Values * are liquid experimentally, but were extrapolated from the solid region of the predominance diagram for comparison purposes. ** Not indicated in experimental results.

T (K)	Transition	log ₁₀ √P Calculated without phonons	log ₁₀ √P Calculated with phonons	log ₁₀ √P Experimental [42]
1000	PdS to Pd ₁₆ S ₇	−1.1	−1.8	−2.2*
1000	Pd ₁₆ S ₇ to Pd ₄ S	−1.4	−2.6	−2.4*
1000	Pd ₄ S to Pd	−3.3	−5.3	−5.2
800	PdS to Pd ₁₆ S ₇	−3.1	−3.5	−3.7
800	Pd ₁₆ S ₇ to Pd ₄ S	−3.5	−4.5	−4.7
800	Pd ₄ S to Pd	−5.9	−7.6	**

results presented in an alternative-but-equivalent format. The SQS estimate for fcc at 50% Pd lies almost directly on this free energy curve, further supporting its usage for quantitative estimates. We also neglect phonon free energy for activity calculations, as for ordered fcc and bcc at 50% Pd, the difference in phonon free energy per atom is only 2 meV at $T = 1000$ K.

Shown below in Fig. 9 in solid lines are our calculated activities for palladium in the Cu–Pd binary, using the free energy models from Table 3, the modified fcc phase, and our calculated data for Cu₃Pd. The β phase is the sharply increasing region in the center of the graph. This sharp behavior is due to the entropic portion of the free energy, which has a logarithmic singularity at $x = 0.5$ and sharply varying derivative near this singularity. The smooth curves on the left and right sides of the graph for $T < 1000$ K denote the fcc phase. Linear free energy functions give constant activities as a function of composition, and thus phase coexistence regimes appear as plateaus in activities, at a fixed temperature. Two sets of plateaus are present. The set of plateaus on the left side are coexistence regimes between the bcc and fcc phases. There are 3 types of plateaus on the right side. For $T < 900$ K, the plateaus are due to coexistence with the line compound Cu₃Pd, where the plateaus in the region $0.6 < x < 0.8$ indicate coexistence with bcc and the plateaus at $0.8 < x < 0.9$ indicate coexistence with fcc. The plateau on the right side of the plot for $T = 900$ K is a special case. Our free energy models predict that the Cu₃Pd phase becomes thermodynamically unstable at 899 K and fcc becomes stable, so the plateau at 900 K indicates coexistence between bcc and fcc. At a temperature of 960 K, our model predicts that the bcc phase becomes unstable relative to the fcc phase, disappearing at a composition of $x = 0.576$. By decreasing the fcc free energy magnitude we have properly stabilized the β phase at temperatures of interest and brought the transition temperature to within 90 K of the expected value. The 1000 K and 1350 K plots are pure fcc throughout the entire composition range.

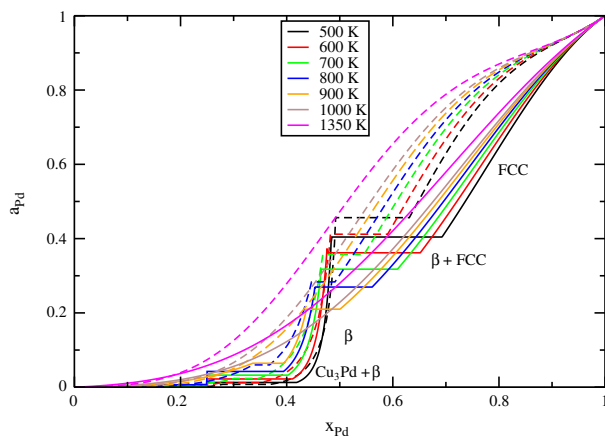


Fig. 9. Activities of Pd in the Cu–Pd binary. First principles results are denoted with solid lines, and CALPHAD with dashed lines.

The activities of Pd at various temperatures were also calculated using CALPHAD (acronym of CALculation of PHase Diagrams) method. The thermodynamic database developed by Li et al. [8] was used. Our activities are systematically low compared to the CALPHAD activities (shown in dashed lines on Fig. 9), most likely due to our ideal entropy approximation. As the true entropy in solid solutions is reduced relative to the ideal entropy, the true free energy will be greater, leading to the true activities being greater than our calculated activities. This is especially true for fcc, where the refitted free energy still overestimates the magnitude of the free energy and leads to qualitatively different behavior in the high Pd limit. CALPHAD results give activities that exceed Raoult's Law in the high Pd limit, which would require positive enthalpies of formation for Cu substitution in Pd using a solid substitution model in the dilute limit. This contradicts first principle calculations which unambiguously predict Cu substitutions in bulk Pd having negative enthalpies of formation (see Fig. 1). Clearly more precise models are needed to understand the binary in the high Pd limit. However, for the β phase and associated coexistence regimes, the first principles and CALPHAD results are in close agreement, and if one is interested in regions outside the single-phase fcc region, first principles calculations gives reasonably accurate results even with simple models.

4. Conclusions

Using only first principles calculations and solid solution models, we were able to semi-quantitatively model the ternary phase diagram for the Cu–Pd–S system without any empirical fitting parameters. We obtained the sulfidization thresholds for the Pd–S₂ system and activities that reflect the essential features of the Cu–Pd binary system at temperatures where multiple phases exist across the composition range. More detailed models are necessary to reach better quantitative agreement with experimental results. However, our work reveals the essential physics underlying the phase behavior. For example, we distinguish enthalpic versus entropic driven substitution, and we identify a pseudogap stabilization mechanism, yielding a temperature-independent solubility range for Cu in Pd₁₆S₇.

Acknowledgements

We are grateful to B. Gleeson, M. Mihalkovič, and J. Kitchin for useful discussion. This technical effort was performed in support of the Fuels Program of Strategic Center for Coal at DOE National Energy Technology Laboratory under the RES contract DE-FE0004000.

References

- [1] C.-H. Chen, Y.H. Ma, *J. Membr. Sci.* 362 (2010) 535–544.
- [2] H. Amandusson, L.-G. Ekedahl, H. Dannetun, *J. Membr. Sci.* 193 (2001) 35–47.
- [3] S. Uemija, T. Matsuda, E. Kikuchi, *J. Membr. Sci.* 56 (1991) 315–325.
- [4] O. Iyoha, R. Enick, R. Killmeyer, B. Morreale, *J. Membr. Sci.* 305 (2007) 77–92.

- [5] C.P. O'Brien, B.H. Howard, J.B. Miller, B.D. Morreale, A.J. Gellman, *J. Membr. Sci.* 349 (2010) 380–384.
- [6] S. Karup-Møller, E. Makovicky, *N. Jb. Miner. Mh.* 12 (1999) 551–567.
- [7] P.R. Subramanian, D.E. Laughlin, *J. Phase Equilib.* 12 (1991) 231–243.
- [8] M. Li, Z. Du, C. Guo, C. Li, *CALPHAD* 32 (2008) 439–446.
- [9] G. Trimarchi, A. Zunger, *J. Phys.-Condens. Mat.* 20 (2008) 295212.
- [10] S. Baärtlelein, E. Winning, G.L.W. Hart, S. Müller, *Acta Mater.* 57 (2009) 1660–1665.
- [11] G. Ceder, D. de Fontaine, H. Dreyse, D.M. Nicholson, G.M. Stocks, B.L. Gyorffy, *Acta Metall. Mater.* 38 (1990) 2299–2308.
- [12] B.J. Lee, B. Sundman, S.I. Kim, K.G. Chin, *ISIJ Int.* 47 (2007) 163–171.
- [13] H. Okamoto, *J. Phase Equilib.* 13 (1992) 106–107.
- [14] G. Kresse, J. Hafner, *Phys. Rev. B* 43 (1993) 558–561.
- [15] G. Kresse, J. Furthmüller, *Phys. Rev. B* 54 (1996) 11169–11186.
- [16] P.E. Blöchl, *Phys. Rev. B* 50 (1994) 17953–17979.
- [17] R. Hu, M.C. Gao, O.N. Doğan, P. King, M. Widom, *CALPHAD* 34 (2010) 324–331.
- [18] J.P. Perdew, A. Ruzsinszky, G.I. Csonka, O.A. Vydrov, G.E. Scuseria, L.A. Constantin, X. Zhou, K. Burke, *Phys. Rev. Lett.* (2008).
- [19] E.J. Wu, G. Ceder, A. van de Walle, *Phys. Rev. B* 67 (2003) 134103.
- [20] E.A. Owen, E.L. Yates, *Philos. Mag.* 15 (1933) 472–487.
- [21] I.R. Harris, M. Norman, W.E. Gardner, *J. Less-Common Met.* 29 (1972) 299–309.
- [22] K. Okamura, *J. Phys. Soc. Jpn.* 28 (1970) 1005–1014.
- [23] H.T. Evans Jr., *Science* 203 (1979) 356–358.
- [24] M. Leon, N. Terao, F. Rueda, *Phys. Status Solidi A* 67 (1981) K11–K14.
- [25] H. Fjellvåg, F. Grnvoid, S. Stlen, A.F. Andresen, R. Müller-Käfer, A. Simon, *Z. Krist.* 184 (1988) 111–121.
- [26] H.E. King, C.T. Prewitt, *Am. Mineral.* 64 (1979) 1265–1271.
- [27] F. Grønvoid, E. Røst, *Acta Cryst.* 15 (1962) 11–13.
- [28] P. Matkovič, M. El-Boragy, K. Schubert, *J. Less-Common Met.* 50 (1976) 165–176.
- [29] T.F. Gaskell, *Z. Kristallogr.* 96 (1937) 203–213.
- [30] F. Grønvoid, E. Røst, *Acta Cryst.* 10 (1957) 329–331.
- [31] A. Janosi, *Acta Cryst.* 17 (1964) 311–312.
- [32] M. Guymont, D. Gratias, *Phys. Status Solidi A* 36 (1976) 329–334.
- [33] E. Røst, *Acta Chem. Scand.* 22 (1968) 819–826.
- [34] A. Soutter, A. Colson, J. Hertz, *Mem. Stud. Sci. Rev. Met.* 68 (1971) 575–591.
- [35] A.H. Geisler, J.B. Newkirk, *J. Met.* 6 (1954) 1076–1082.
- [36] K. Yamamoto, S. Kashida, *J. Solid State Chem.* 93 (1991) 202–211.
- [37] D. Topa, E. Makovicky, T. Balić-Žunić, *Can. Mineral.* 44 (2006) 497–505.
- [38] E. Bruno, B. Ginatempo, E.S. Giuliano, *Phys. Rev. B* 63 (2001) 174107.
- [39] C. Wolverton, *Acta Mater.* 49 (2001) 3129–3142.
- [40] J. Friedel, *Helv. Phys. Acta* 61 (1988) 538–555.
- [41] J.M.W. Chase, *J. Phys. Chem. Ref. Data* 9 (1998) 1–1951.
- [42] J.R. Taylor, *Met. Trans. B* 16B (1985) 143–148.
- [43] R. DeHoff, *Thermodynamics in Materials Science*, second ed., CRC Press, 2006.